Electronic Supplementary Material (ESI) for Dalton Transactions.

Supplementary Information

Heterometallic molecular precursors for lithium-iron oxide material: synthesis, solid state structure, solution and gas-phase behavior, and thermal decomposition

Haixiang Han,[a] Zheng Wei,[a] Matthew C. Barry,[a] Alexander S. Filatov[b] and Evgeny V. Dikarev*[a]

[a]*Department of Chemistry, University at Albany, SUNY, Albany, NY, United States*

[b]*Department of Chemistry, University of Chicago, Chicago, IL, United States*

*Author to whom correspondence should be addressed. E-mail: edikarev@albany.edu. Phone: (518)442-4401. Fax: (518)442-3462.

Content

Experimental Section. General Procedures……...S3

Synthesis of Starting Reagents……..S4

Synthesis of Heterometallic Precursors **1**-**4**……..…….S5

X-ray Powder Diffraction Patterns of Starting Reagents…..……..……...……....S8

X-ray Powder Diffraction Patterns of Heterometallic Compounds **1**-**4**…….…...……....S9

Crystal Growth…..…….……..S14

X-ray Crystallographic Procedures……..……..…….....S15

Solid State Structures of Heterometallic Compounds **1**-**4** and $Mg(tbaoac)_2$……...S18

ATR-IR Spectra of Heterometallic Compounds **1**-**4**……...S27

^{1}H and ^{7}Li NMR Spectra of $LiMg(tbaoac)_3$ (**4**)…...……..……..S29

DART Mass Spectra of Heterometallic Compounds **1**, **2**, and **4**…….……..…..S31

Thermal Decomposition of Heterometallic Precursors……..…….S37

References……S40

Experimental Section. General Procedures

All of the manipulations were carried out in a dry, oxygen-free argon atmosphere by employing standard Schlenk and glove box techniques. Anhydrous iron (II) chloride ($FeCl_2$), magnesium chloride ($MgCl_2$), lithium methoxide (LiOMe), lithium acetylacetonate (Li(acac)), lithium bis(trimethylsilyl) amide, *tert*-butyl acetoacetate (Htbaoac), and 1,1,1-trifluoro-5,5-dimethyl-2,4-hexanedione (Hptac) were purchased from Sigma-Aldrich and used upon received. Li(tbaoac) was prepared according to the literature synthesis procedure.[1] In addition, Li(tbaoac) can also be prepared by the procedure described in the next section. The attenuated total reflection (ATR) spectra were recorded on a PerkinElmer Spectrum 100FT-IR spectrometer. NMR spectra were obtained on a Bruker Advance 400 spectrometer at 400 MHz for ^{1}H and at 155.5 MHz for ^{7}Li. Chemical shifts (δ) are given in ppm relative to the residual solvent peaks for ^{1}H and to the ^{7}Li peak of external standard (0.1 M solution of LiCl in D_2O). Mass spectra were acquired using a DART-SVP ion source (IonSense, Saugus, MA, USA) coupled to a JEOL AccuTOF time-of-flight mass spectrometer (JEOL USA, Peabody, MA, USA) in positive ion mode. Spectra were recorded over the mass range of *m*/*z* 200–2000 at one spectrum per second with a gas heater temperature of 350 °C. Thermal decomposition of heterometallic precursors was studied in air at ambient pressure. The solid sample (*ca*. 40 mg) was placed into a 20 mL Coors high-alumina crucible (Aldrich) and heated at a rate of *ca.* 35 °C/min in a muffle furnace (Lindberg Blue M). The decomposition residues were analyzed by X-ray powder diffraction. X-ray powder diffraction data were collected on a Bruker D8 Advance diffractometer (Cu Kα radiation, focusing Göbel Mirror, LynxEye one-dimensional detector, step of 0.02º 2θ, 20 °C). The crystalline samples under investigation were ground and placed in the dome-like airtight zero-background holders. Le Bail fit for powder diffraction patterns has been performed using TOPAS, version 4 software package (Bruker AXS, 2006).

Synthesis of Starting Reagents

Li(tbaoac). A flask was charged with lithium bis(trimethylsilyl) amide (3.027 g, 18.09 mmol) under argon atmosphere, and 40 mL dry, oxygen-free hexanes were added. Upon stirring, Htbaoac (2.862 g, 3.00 mL) was added to the solution. The solution was stirred for 0.5 h, while white precipitate was forming gradually. The solid was filtered off and washed several times with hexanes. The final white product was obtained by drying the residue under vacuum at 100 ^{o}C overnight. Yield was 2.851 g (96%). ^{1}H NMR (400 MHz, $CDCl_3$, 22 ^{o}C): δ 1.40 (s, OC(CH_3)$_3$); 1.94 (s, CH_3); 4.78 (s, CH). ^{7}Li NMR (155.5 MHz, THF, 22 °C): δ 1.26 (s), (155.5 MHz, DMSO, 22 °C): δ 3.42 Compound is soluble in all common solvents, except hexanes. It can be recrystallized by cooling down its saturated solution in dichloromethane at -10 °C overnight. Compound starts to decompose at *ca.* 180 °C in evacuated ampule, before any sublimation is visually observed.

Li(ptac). A flask was charged with LiOMe (0.656 g, 17.26 mmol) under argon atmosphere, and 40 mL of dry, oxygen-free methanol were added. Upon stirring, Hptac (3.387 g, 3.00 mL) was added to the solution. The colorless solution was stirred at room temperature for 1 h. The solvent was evaporated under vacuum at room temperature. The white-colored final product was obtained by further drying the residue under vacuum at 80 ^{o}C overnight. Yield was 3.315 g (95%). ^{1}H NMR (400 MHz, d_6-acetone, 22 ^{o}C): δ 1.09 (s, C(CH_3)$_3$); 5.67 (s, CH). The purity of the crystalline product was confirmed by X-ray powder diffraction analysis (Figure S1 and Table S1).

Fe(tbaoac)$_2$. The synthetic procedure was similar to the synthesis of Co(tbaoac)$_2$ that we reported earlier.[1] Anhydrous $FeCl_2$ (1.148 g, 9.04 mmol) was dissolved in 20 mL of ethanol. Upon stirring, a solution of Htbaoac (3.00 mL, 18.1 mmol) in 5 mL of ethanol was added. The solution of triethylamine (2.52 mL, 18.1 mmol) in 5 mL of ethanol was added dropwise to the reaction mixture. The solution was stirred for 0.5 h. The solvent was evaporated and the solid was washed several times with hexanes. The final brown product was obtained by drying the residue under vacuum at 100 °C overnight. Yield was 3.111 g (93%). Compound is soluble in all common solvents, except hexanes.

Mg(tbaoac)$_2$. Anhydrous $MgCl_2$ (0.859 g, 9.04 mmol) was dissolved in 20 mL of water. Upon stirring, a solution of Htbaoac (3.00 mL, 18.1 mmol) in 5 mL of ethanol was added. The solution of triethylamine (2.52 mL, 18.1 mmol) in 5 mL of ethanol was added dropwise to the reaction mixture. The resulting solution was stirred for 0.5 h, while white precipitate was forming gradually. The solid was filtered off and washed several times with water and cold ethanol. The final white product was obtained by drying the residue under vacuum at 100 °C overnight. Yield was 2.937 g (96%). ^{1}H NMR (400 MHz, $CDCl_3$, 22 ^{o}C): δ 1.4050 (s, C(CH_3)$_3$); 1.7174 (s, CH_3); 4.6469 (s, CH). ^{1}H NMR (400 MHz, d_6-DMSO, 22 ^{o}C): δ 1.2954 (s, C(CH_3)$_3$); 1.6043 (s, CH_3); 4.3351 (s, CH). Compound is soluble in all common solvents, except hexanes and water. The purity of the crystalline product was confirmed by X-ray powder diffraction analysis (Figure S2 and Table S2).

Synthesis of Heterometallic Precursors 1-4

LiFe(tbaoac)$_3$ (1).

Method I. A mixture of Li(tbaoac) (57 mg, 0.35 mmol) and anhydrous $FeCl_2$ (15 mg, 0.12 mmol) was sealed in an evacuated glass ampule and was kept in an electric furnace without temperature gradient at 125 ^{o}C for 3 days. The resulting yellow product was quantitatively resublimed at 105 ^{o}C under dynamic vacuum conditions (cold finger). Yield was 54 mg (85 %). Compound **1** decomposes at the temperatures higher than 175 ^{o}C and is soluble in all common solvents. The purity of the bulk crystalline product was confirmed by X-ray powder diffraction analysis (Figure S3 and Table S3).

Method II. A flask was loaded with Li(tbaoac) (0.391 g, 2.36 mmol) and anhydrous $FeCl_2$ (0.100 g, 0.787 mmol) under argon atmosphere, and 100 mL of dry ethanol was added. The yellow solution was stirred at room temperature for 1 h. The solvent was evaporated under vacuum at room temperature, and the yellow solid residue was further dried under vacuum at 100 ^{o}C overnight. The final yellow product was isolated by dichloromethane extraction followed by evaporation of the solvent at room temperature. Yield was 0.400 g (95 %).

Method III. A flask was loaded with Li(tbaoac) (0.500 g, 3.05 mmol) and $Fe(tbaoac)_2$ (1.119 g, 3.04 mmol) under argon atmosphere, and 50 mL of dry, oxygen-free dichloromethane was added. The yellow solution was stirred at room temperature for 1 h. The solvent was evaporated under vacuum at room temperature. Yield was 1.453 g (90%).

$LiFe(ptac)_3$ (2).

Method I. A mixture of Li(ptac) (72 mg, 0.35 mmol) and anhydrous $FeCl_2$ (15 mg, 0.12 mmol) was sealed in an evacuated glass ampule and placed in an electric furnace having a temperature gradient along the length of the tube. The ampule was kept at 125 ^oC for 3 days to allow block-shaped orange crystals to be deposited in the cold section of the container where the temperature was set approximately 5 ^oC lower. Yield was 66 mg (86 %). Compound **2** is soluble in all common solvents. It can be quantitatively resublimed at 115 ^oC in an evacuated ampule and it is getting decomposed at the temperatures higher than 165 ^oC. The purity of the bulk crystalline product was confirmed by X-ray powder diffraction analysis (Figure S4 and Table S4).

Method 1I. A flask was loaded with Li(ptac) (0.478 g, 2.36 mmol) and anhydrous $FeCl_2$ (0.100 g, 0.787 mmol) under argon atmosphere, and 100 mL of dry ethanol was added. The orange solution was stirred at room temperature for 1 h. The solvent was evaporated under vacuum at room temperature and the orange solid residue was further dried under vacuum at 100 ^oC overnight. The final orange product was isolated by dichloromethane extraction followed by evaporation of the solvent at room temperature. Yield was 0.465 g (91 %).

$LiFe(acac)_3$ (3).

A mixture of Li(acac) (38 mg, 0.35 mmol) and anhydrous $FeCl_2$ (15 mg, 0.12 mmol) was sealed in an evacuated glass ampule and placed in an electric furnace having a temperature gradient along the length of the tube. The ampule was kept at 125 ^oC for 7 days to allow needle-shaped yellow crystals to be deposited in the cold section of the container where the temperature was set approximately 5 ^oC lower. Yield was 36 mg (84 %). The purity of the bulk crystalline product was confirmed by X-ray powder diffraction analysis (Figure S5 and Table S5).

$LiMg(tbaoac)_3$ (4).

Method I. A mixture of Li(tbaoac) (78 mg, 0.47 mmol) and anhydrous $MgCl_2$ (15 mg, 0.16 mmol) was sealed in an evacuated glass ampule and placed in an electric furnace without temperature gradient at 155 ^oC for 3 days. The final product was quantitatively resublimed at 145 ^oC under dynamic vacuum conditions (cold finger). Yield was 60 mg (75 %). Compound **4** is decomposed at the temperatures higher than 165 ^oC and is soluble in all common solvents except hexanes. The purity of the bulk crystalline product was confirmed by X-ray powder diffraction analysis (Figure S6 and Table S6).

Method II. A flask was loaded with anhydrous $MgCl_2$ (0.500 g, 5.26 mmol) and Li(tbaoac) (2.592 g, 15.79 mmol) under argon atmosphere, and 100 mL of dry, oxygen-free ethanol was added. The colorless solution was stirred at room temperature for 1 h. The solvent was evaporated under vacuum at room temperature, and the white solid residue was further dried under vacuum at 80 °C overnight. The final white product was isolated by dichloromethane extraction flowed by evaporation of the solvent at room temperature. Yield was 2.407 g (91%).

Method III. A flask was loaded with Li(tbaoac) (0.500 g, 3.05 mmol) and $Mg(tbaoac)_2$ (1.030 g, 3.04 mmol) under argon atmosphere, and 50 mL of dry, oxygen-free dichloromethane was added. The colorless solution was stirred at room temperature for 1 h. The solvent was evaporated under vacuum at room temperature. Yield was 1.454 g (95%).

X-ray Powder Diffraction Patterns of Starting Reagents

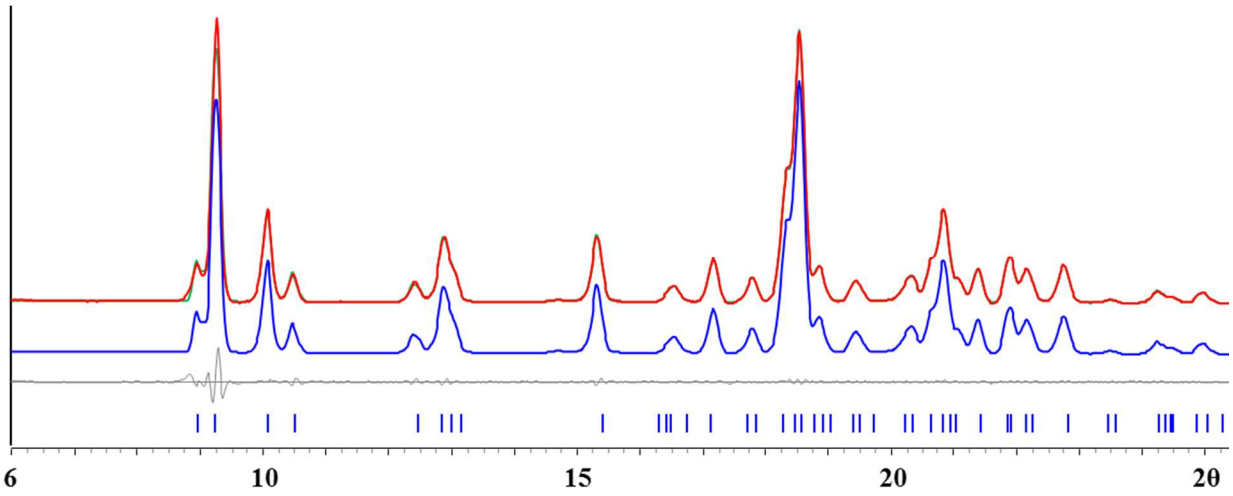

Figure S1. X-ray powder diffraction pattern of Li(ptac) and the Le Bail fit. The red and green curves are experimental and calculated patterns overlaid. The blue curve is calculated pattern. Grey line is the difference curve. Theoretical peak positions are shown at the bottom as blue lines.

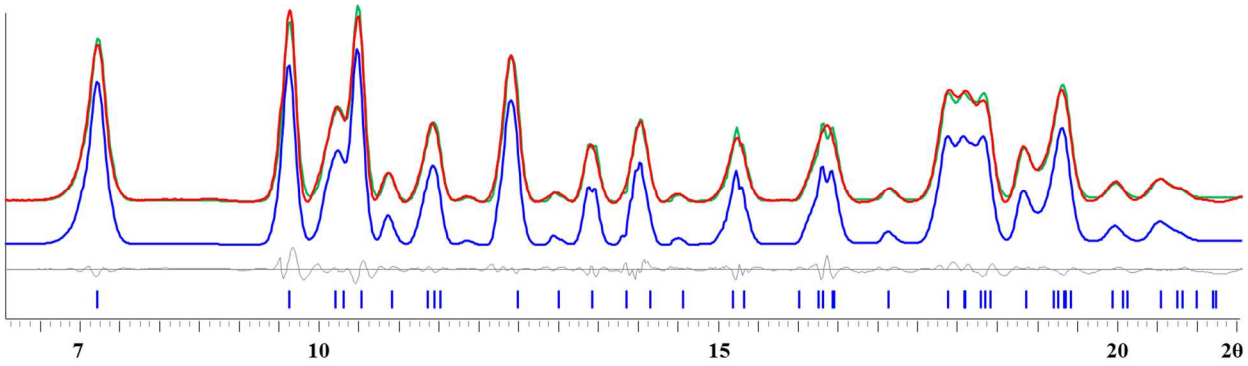

Figure S2. X-ray powder diffraction pattern of $Mg(tbaoac)_2$ and the Le Bail fit. The red and green curves are experimental and calculated patterns overlaid. The blue curve is calculated pattern. Grey line is the difference curve. Theoretical peak positions are shown at the bottom as blue lines.

X-ray Powder Diffraction Patterns of Heterometallic Compounds 1-4

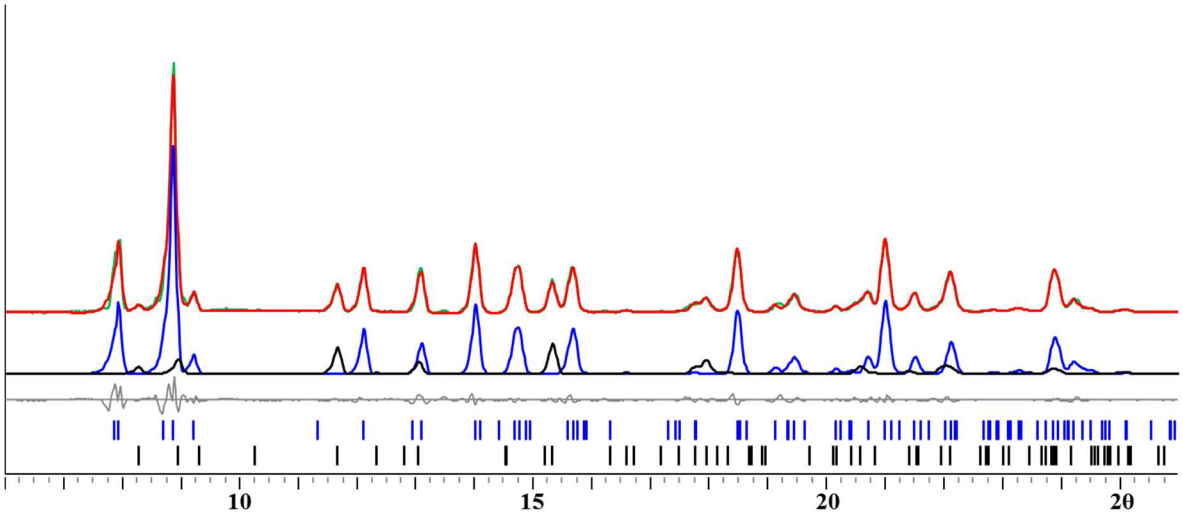

Figure S3. X-ray powder diffraction pattern of $LiFe(tbaoac)_3$ (**1**) and the Le Bail fit. The red and green curves are experimental and calculated patterns overlaid. The blue and black curves are calculated single peak patterns for two polymorph modifications with theoretical peak positions shown at the bottom as blue and black lines (triclinic and monoclinic modifications, respectively). Grey line is the difference curve.

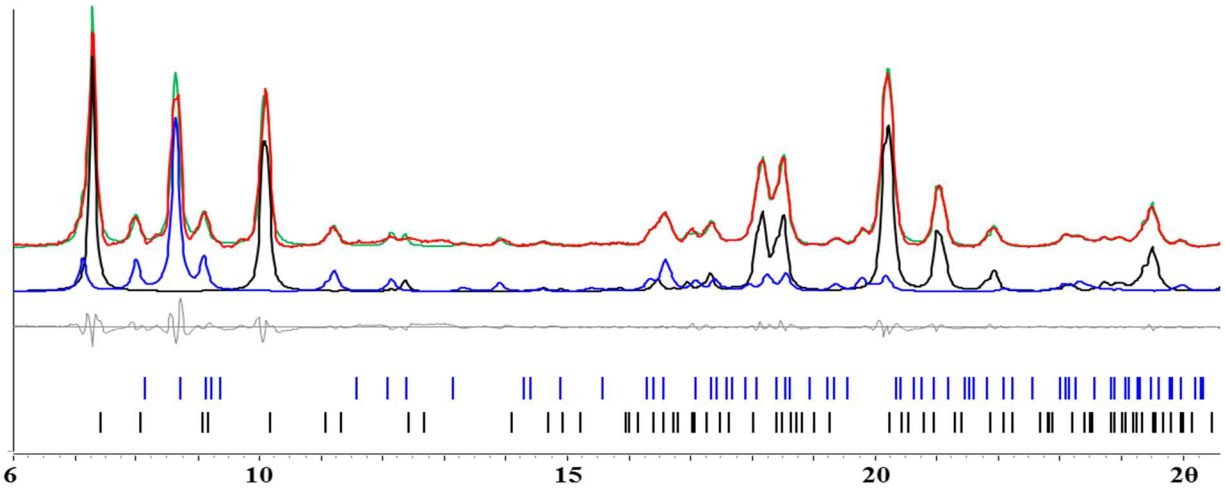

Figure S4. X-ray powder diffraction pattern of $LiFe(ptac)_3$ (**2**) and the Le Bail fit. The red and green curves are experimental and calculated patterns overlaid. The blue and black curves are calculated single peak patterns for two polymorph modifications with theoretical peak positions shown at the bottom as blue and black lines (triclinic and monoclinic modifications, respectively). Grey line is the difference curve.

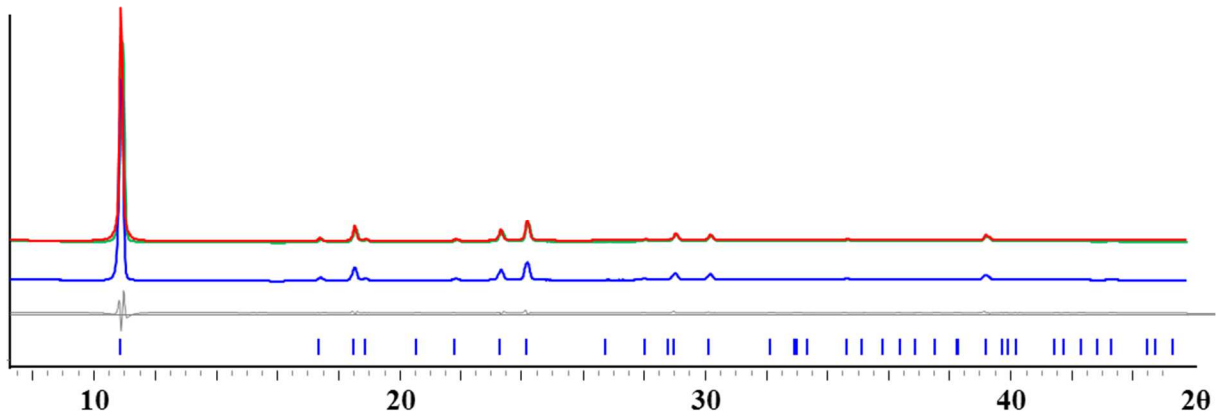

Figure S5. X-ray powder diffraction pattern of $LiFe(acac)_3$ (**3**) and the Le Bail fit. The red and green curves are experimental and calculated patterns overlaid. The blue curve is calculated pattern. Grey line is the difference curve. Theoretical peak positions are shown at the bottom as blue lines.

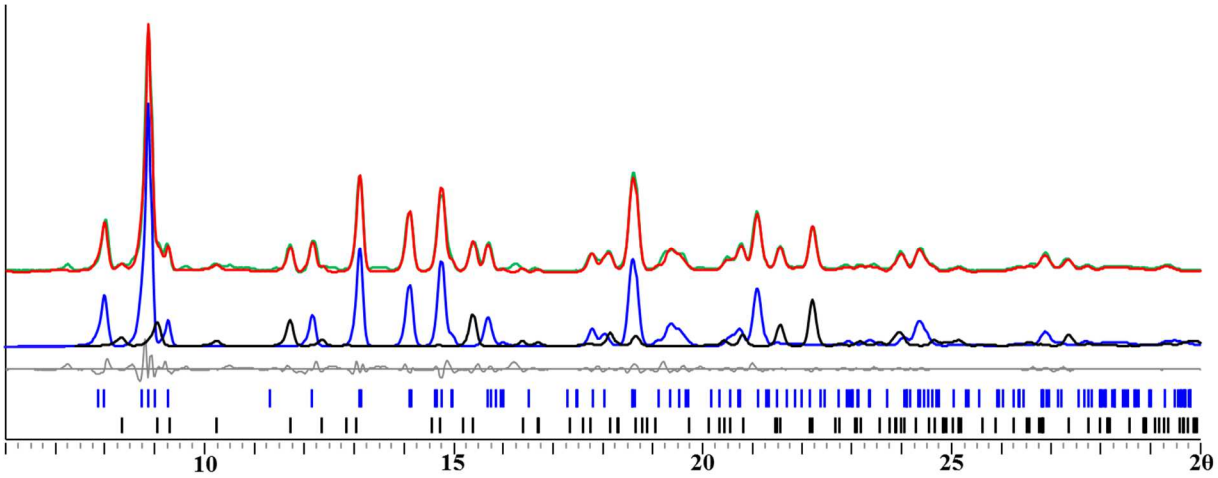

Figure S6. X-ray powder diffraction pattern of $LiMg(tbaoac)_3$ (**4**) and the Le Bail fit. The red and green curves are experimental and calculated patterns overlaid. The blue and black curves are calculated single peak patterns for two polymorph modifications with theoretical peak positions shown at the bottom as blue and black lines (triclinic and monoclinic modifications, respectively). Grey line is the difference curve.

Table S1. Unit Cell Parameters for Li(ptac) Obtained by the Le Bail Fit and from the Single Crystal Data

Li(ptac)		
	Le Bail fit (20 °C)	Single Crystal Data (-173 °C)[2]
Sp. Gr.	*Pbca*	*Pbca*
a (Å)	19.542(2)	19.154(4)
b (Å)	10.985(2)	10.723(2)
c (Å)	19.945(2)	19.801(4)
V (Å^3)	4281.6(5)	4066.1(5)

Table S2. Unit Cell Parameters for $Mg(tbaoac)_2$ Obtained by the Le Bail Fit and from the Single Crystal Data

$Mg(tbaoac)_2$		
	Le Bail fit (20 °C)	Single Crystal Data (-173 °C)
Sp. Gr.	$P2_1/n$	$P2_1/n$
a (Å)	9.782(2)	9.7090(8)
b (Å)	17.348(2)	17.0101(14)
c (Å)	17.721(2)	17.5059(15)
β (°)	101.025(2)	101.082(2)
V (Å^3)	2951.4(6)	2837.2(4)

Table S3. Unit Cell Parameters for $LiFe(tbaoac)_3$ (**1**) Obtained by the Le Bail Fit and from the Single Crystal Data

$LiFe(tbaoac)_3$ (**1**)			
	Le Bail fit (20 °C)		Single Crystal Data (-173 °C)
Sp. Gr.	$P2_1/n$	P-1	P-1
a (Å)	12.230(4)	11.684(1)	11.643(2)
b (Å)	9.690(2)	12.562(1)	12.253(2)
c (Å)	19.053(5)	12.983(1)	12.534(2)
α (°)	90	102.642(1)	103.777(2)
β (°)	94.90(2)	106.471(1)	106.650(2)
γ (°)	90	112.163(1)	111.299(2)
V (Å^3)	2249.7(8)	1574.4(1)	1474.2(5)

Table S4. Unit Cell Parameters for $LiFe(ptac)_3$ (**2**) Obtained by the Le Bail Fit and from the Single Crystal Data

$LiFe(ptac)_3$ (**2**)			
	Le Bail fit (20 °C)		Single Crystal Data (-173 °C)
Sp. Gr.	$C2/c$	P-1	P-1
a (Å)	17.587(2)	11.424(2)	11.3877(11)
b (Å)	12.624(2)	11.896(2)	11.8362(11)
c (Å)	24.348(2)	12.154(1)	11.9720(11)
α (°)	90	91.641(1)	91.399(2)
β (°)	91.67(2)	113.048 1)	113.519(2)
γ (°)	90	101.813(1)	100.038(2)
V (Å^3)	5403.4(5)	1476.8(5)	1449.1(1)

Table S5. Unit Cell Parameters for $LiFe(acac)_3$ (**3**) Obtained by the Le Bail Fit and from the Single Crystal Data

$LiFe(acac)_3$ (**3**)		
	Le Bail fit (20 °C)	Single Crystal Data (-173 °C)
Sp. Gr.	*R*-3*c*	*R*-3*c*
a (Å)	16.402(2)	16.352(3)
c (Å)	11.018(2)	10.8897(16)
V (Å^3)	2567.1(8)	2521.7(12)

Table S6. Unit Cell Parameters for $LiMg(tbaoac)_3$ (**4**) Obtained by the Le Bail Fit and from the Single Crystal Data

$LiMg(tbaoac)_3$ (**4**)			
	Le Bail fit (20 °C)		Single Crystal Data (-173 °C)
Sp. Gr.	$P2_1/n$	*P*-1	*P*-1
a (Å)	12.089(1)	11.641(2)	11.556(5)
b (Å)	9.695(2)	12.614(2)	12.211(5)
c (Å)	19.087(5)	12.938(1)	12.471(5)
α (°)	90	103.011(1)	103.660(5)
β (°)	95.21(2)	105.954(1)	106.731(5)
γ (°)	90	112.691(1)	111.403(5)
V (Å^3)	2227.8(2)	1563.5(2)	1449.6(10)

Crystal growth

Block-shaped crystals of $LiFe(tbaoac)_3$ (**1**) suitable for structural measurements were obtained by keeping its saturated dichloromethane solution at around -20 °C for 2 days. Crystals of $LiFe(ptac)_3$ (**2**) and $LiFe(acac)_3$ (**3**) were grown by sublimation in evacuated glass ampules placed in an electric furnace at 125 °C with a temperature gradient of approximately 5 °C along the length of container. Single crystals of $LiMg(tbaoac)_3$ (**4**) were immediately losing their crystallinity upon removal from the dichloromethane solution, therefore a mixture of dichloromethane/dichloroethane (volume ratio = 1:1) was used to grow suitable single crystals in a freezer at -20 °C. Colorless block-shaped crystals of homometallic complex $Mg(tbaoac)_2$ were prepared by slow evaporation of its saturated dichloromethane solution at room temperature.

Table S7. Single Crystal Growth Conditions

Compound	**1**	**2**	**3**	**4**	$Mg(tbaoac)_2$
Shape	Block	Block	Needle	Block	Block
Color	Yellow	Orange	Yellow	Colorless	Colorless
Time	2 days	3 days	14 days	7 days	3 days
Method	CH_2Cl_2 solution	Sublimation	Sublimation	$CH_2Cl_2/C_2H_4Cl_2$ solution	CH_2Cl_2 solution/ slow evaporation
Temperature	-20 °C	125 °C	125 °C	-20 °C	20 °C

X-ray Crystallographic Procedures

The single crystal diffraction data for $LiFe(tbaoac)_3$ (**1**) and $LiMg(tbaoac)_3$ (**4**) were measured on a Bruker SMART APEX CCD based X-ray diffractometer system equipped with a Mo-target X-ray tube (λ = 0.71073 Å). The single crystal diffraction data for $Mg(tbaoac)_2$, $LiFe(ptac)_3$ (**2**), and $LiFe(acac)_3$ (**3**) were collected on a Bruker D8 VENTURE with PHOTON 100 CMOS detector system using Mo radiation (λ = 0.71073 Å). Data reduction and integration were performed with the Bruker software package SAINT. Data were corrected for absorption effects using the empirical methods as implemented in SADABS. The structures were solved and refined by full-matrix least-squares procedures using the Bruker SHELXTL (version 6.14) software package. All non-hydrogen atoms were refined anisotropically and hydrogen atoms were included in idealized positions for structure factor calculations. One of the CF_3 groups in $LiFe(ptac)_3$ (**2**) was found to be rotationally disordered. All fluorine atoms of the disordered parts were modeled with isotropic thermal parameters using similarity restraints. Some bond distances in the disordered moieties were also restrained. Crystallographic data for all compounds and details of the data collection and structure refinement are listed in Table S8.

Table S8. Crystal Data and Structure Refinement Parameters for $LiFe(tbaoac)_3$ (**1**), $LiFe(ptac)_3$ (**2**), $LiFe(acac)_3$ (**3**), $LiMg(tbaoac)_3$ (**4**), and $Mg(tbaoac)_2$

Compound	**1**	**2**	**3**
Empirical formula	$C_{48}H_{78}Li_2Fe_2O_{18}$	$C_{48}H_{60}F_{18}Li_2Fe_2O_{12}$	$C_{15}H_{21}LiFeO_6$
Formula weight	1068.68	1296.54	360.11
Temperature (K)	100(2)	100(2)	100(2)
Wavelength (Å)	0.71073	0.71073	0.71073
Crystal system	Triclinic	Triclinic	Trigonal
Space group	*P*-1	*P*-1	*R*-3*c*
a (Å)	11.643(2)	11.3877(11)	16.352(3)
b (Å)	12.253(2)	11.8362(11)	16.352(3)
c (Å)	12.534(2)	11.9720(11)	10.8897(16)
α (°)	103.777(2)	91.399(2)	90.00
β (°)	106.650(2)	113.519(2)	90.00
γ (°)	111.299(2)	100.038(2)	120.00
V (Å^3)	1474.2(5)	1449.1(2)	2521.7(12)
Z	1	1	6
ρ_{calcd} (g·cm^{-3})	1.204	1.486	1.432
μ (mm^{-1})	0.554	0.614	0.922
F(000)	568	664	1128
Crystal size (mm)	0.46×0.32×0.26	0.18×0.08×0.08	0.21×0.18×0.09
θ range for data collection (°)	2.69-27.01	2.87-28.68	4.01-30.11
Reflections collected	17647	70343	8441
Independent reflections	6423 [R_{int} = 0.0223]	7452 [R_{int} = 0.0437]	841 [R_{int} = 0.0378]
Transmission factors (min/max)	0.7846/0.8693	0.8976/0.9526	0.8300/0.9217
Data/restraints/params.	6432/0/328	7452/18/387	841/0/39
*R*1,[a] *wR*2[b] ($I > 2\sigma(I)$)	0.0324/0.0814	0.0487/0.1104	0.0255/0.0609
*R*1,[a] *wR*2[b] (all data)	0.0371/0.0848	0.0637/0.1189	0.0328/0.0634
Quality-of-fit[c]	1.059	1.073	1.073
Largest diff. peak and hole (ē·Å^{-3})	0.384 and -0.340	0.784 and -0.641	0.377 and -0.207

[a]$R1 = \Sigma||F_o|-|F_c||/\Sigma|F_o|$. [b]$wR2 = [\Sigma[w(F_o^2-F_c^2)^2]/\Sigma[w(F_o^2)^2]]$.
[c]Quality-of-fit = $[\Sigma[w(F_o^2-F_c^2)^2]/(N_{obs}-N_{params})]^{½}$, based on all data.

Compound	**4**	$Mg(tbaoac)_2$
Empirical formula	$C_{48}H_{78}Li_2Mg_2O_{18}$	$C_{48}H_{78}Mg_3O_{18}$
Formula weight	1005.60	1016.03
Temperature (K)	100 (2)	100 (2)
Wavelength (Å)	0.71073	0.71073
Crystal system	Triclinic	Monoclinic
Space group	*P*-1	$P2_1/n$
a (Å)	11.556(5)	9.7090(8)
b (Å)	12.211(5)	17.0101(14)
c (Å)	12.471(5)	17.5059(15)
α (°)	103.660(5)	90.00
β (°)	106.731(5)	101.082(2)
γ (°)	111.403(5)	90.00
V (Å^3)	1449.6(10)	2837.2(4)
Z	1	2
ρ_{calcd} (g·cm^{-3})	1.152	1.189
μ (mm^{-1})	0.105	0.118
F(000)	540	1092
Crystal size (mm)	0.26×0.18×0.12	0.26×0.10×0.07
θ range for data collection (°)	2.13-23.42	2.90-30.45
Reflections collected	22717	82688
Independent reflections	6090 [R_{int} = 0.0561]	8695 [R_{int} = 0.0664]
Transmission factors (min/max)	0.9732/0.9875	0.9698/0.9918
Data/restraints/params.	6090/0/324	8695/0/325
*R*1,[a] *wR*2[b] ($I > 2\sigma(I)$)	0.0503/0.1284	0.0473/0.0950
*R*1,[a] *wR*2[b] (all data)	0.0801/0.1439	0.0879/0.1089
Quality-of-fit[c]	1.032	1.030
Largest diff. peak and hole (ē·Å^{-3})	0.561 and -0.488	0.410 and -0.229

[a] $R1 = \Sigma||F_o|-|F_c||/\Sigma|F_o|$. [b] $wR2 = [\Sigma[w(F_o^2-F_c^2)^2]/\Sigma[w(F_o^2)^2]]$.

[c] Quality-of-fit = $[\Sigma[w(F_o^2-F_c^2)^2]/(N_{obs}-N_{params})]^{½}$, based on all data.

Solid State Structures of Heterometallic Compounds 1-4 and Mg(tbaoac)$_2$

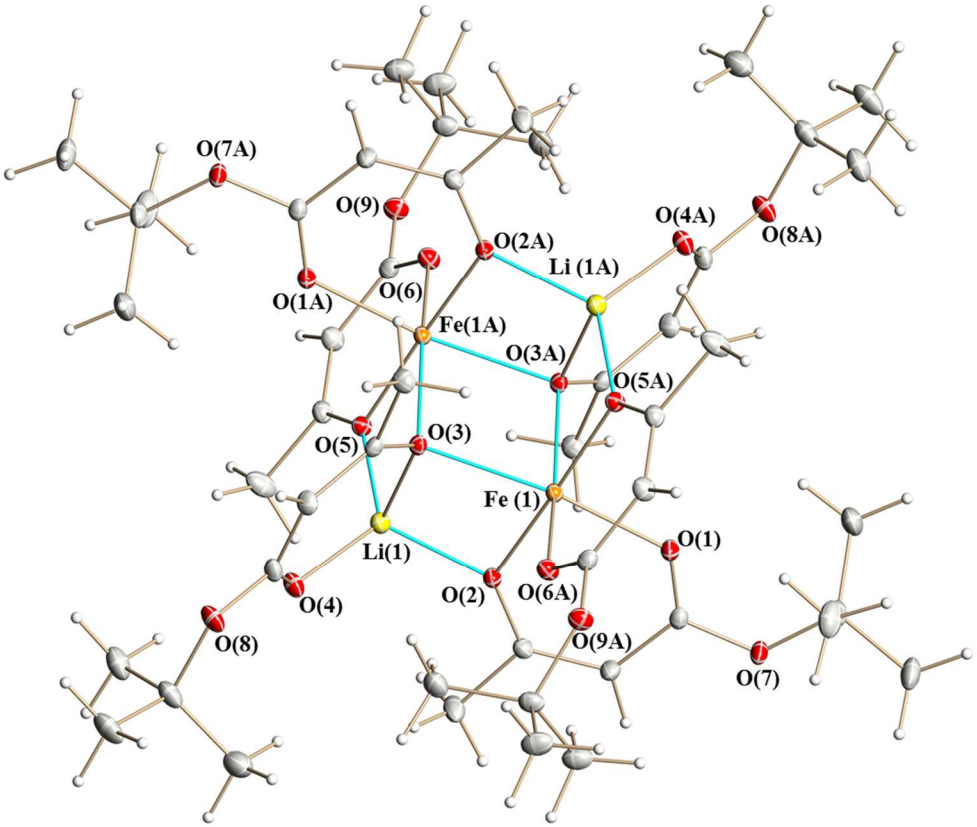

Figure S7. Solid state structure of heterometallic complex $Li_2Fe_2(tbaoac)_6$ (**1**) drawn with thermal ellipsoids at the 40% probability level. Hydrogen atoms are represented by spheres of arbitrary radius. Only metal and oxygen atoms are labeled. The lithium-oxygen and iron-oxygen bonds to the tbaoac ligands involved in bridging interactions are shown in blue.

Table S9. Selected Bond Distances (Å) and Angles (deg.) in the Structure of $Li_2Fe_2(tbaoac)_6$ (**1**)

Bond distances		**Angles**		**Angles**	
Fe(1)–O(1)	2.0748(10)	O(1)–Fe(1)–O(3)	165.31(4)	O(2)–Li(1)–O(3)	91.87(11)
Fe(1)–O(2)**	2.0507(10)	O(1)–Fe(1)–O(3A)	92.65(4)	O(2)–Li(1)–O(5)	117.67(13)
Fe(1)–O(3)*	2.1986(10)	O(1)–Fe(1)–O(6A)	94.02(4)	O(4)–Li(1)–O(2)	125.77(14)
Fe(1)–O(3A)*	2.2194(10)	O(2)–Fe(1)–O(1)	85.88(4)	O(4)–Li(1)–O(3)	99.12(12)
Fe(1)–O(5A)**	2.0435(10)	O(2)–Fe(1)–O(3)	81.53(4)	O(4)–Li(1)–O(5)	114.72(13)
Fe(1)–O(6A)	2.0853(10)	O(2)–Fe(1)–O(3A)	85.55(4)	O(5)–Li(1)–O(3)	91.50(11)
		O(2)–Fe(1)–O(6)	95.39(4)		
Li(1)–O(2)*	1.901(3)	O(3)–Fe(1)–O(3A)	81.65(4)		
Li(1)–O(3)**	1.963(3)	O(5A)–Fe(1)–O(1)	96.38(4)		
Li(1)–O(4)	1.854(3)	O(5A)–Fe(1)–O(2)	177.49(4)		
Li(1)–O(5)*	1.909(3)	O(5A)–Fe(1)–O(3)	96.09(4)		
		O(5A)–Fe(1)–O(3A)	81.07(4)		
		O(5A)–Fe(1)–O(6A)	85.55(4)		
		O(8A)–Fe(1)–O(3)	94.66(4)		
		O(8A)–Fe(1)–O(3A)	165.63(4)		

* – bridging oxygen; ** – chelating-bridging oxygen

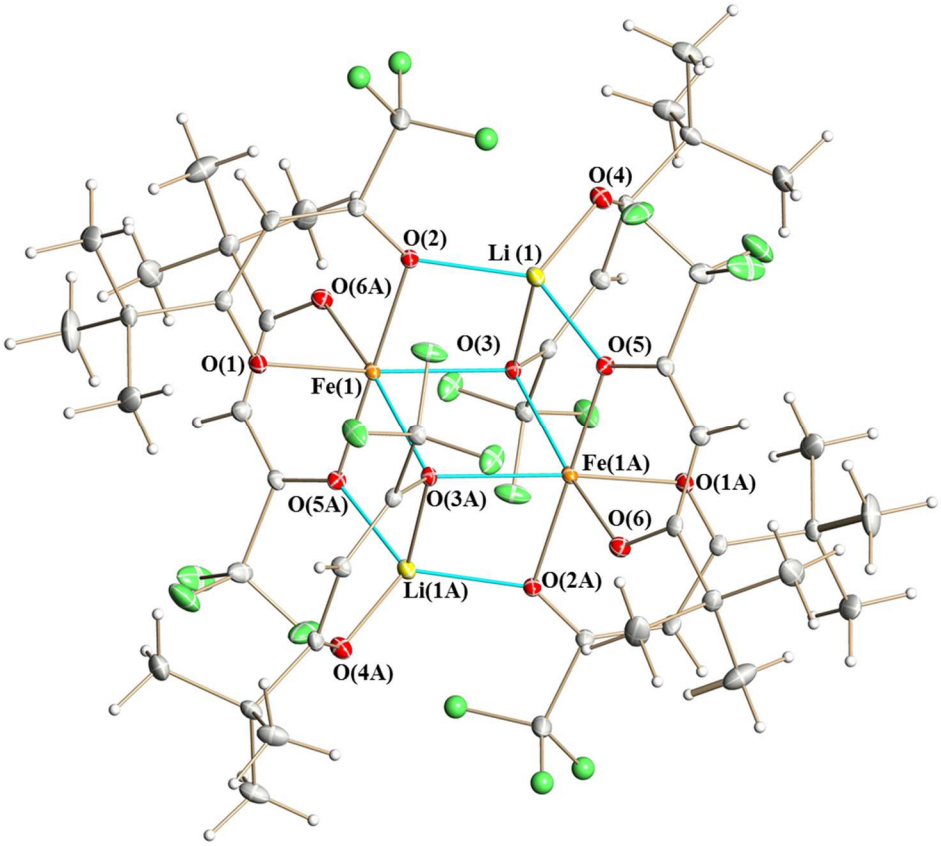

Figure S8. Solid state structure of heterometallic complex $Li_2Fe_2(ptac)_6$ (**2)** drawn with thermal ellipsoids at the 40% probability level. Hydrogen atoms and disordered fluorine atoms are represented by spheres of arbitrary radii. Only metal and oxygen atoms are labeled. The lithium-oxygen and iron-oxygen bonds to the ptac ligands involved in bridging interactions are shown in blue.

Table S10. Selected Bond Distances (Å) and Angles (deg.) in the Structure of $Li_2Fe_2(ptac)_6$ (**2**)

Bond distances		**Angles**		**Angles**	
Fe(1)–O(1)	2.0305(16)	O(1)–Fe(1)–O(3)	163.86(6)	O(4)–Li(1)–O(2)	117.6(2)
Fe(1)–O(2)**	2.0466(15)	O(1)–Fe(1)–O(3A)	92.79(6)	O(4)–Li(1)–O(5)	114.2(2)
Fe(1)–O(3)*	2.2030(15)	O(1)–Fe(1)–O(6A)	92.83(7)	O(2)–Li(1)–O(5)	128.2(2)
Fe(1)–O(3A)*	2.2693(15)	O(2)–Fe(1)–O(1)	86.03(6)	O(4)–Li(1)–O(3)	97.14(18)
Fe(1)–O(5A)**	2.0392(15)	O(2)–Fe(1)–O(3)	81.93(6)	O(2)–Li(1)–O(3)	87.88(16)
Fe(1)–O(6A)	2.0511(16)	O(2)–Fe(1)–O(3A)	100.48(6)	O(5)–Li(1)–O(3)	88.12(16)
		O(2)–Fe(1)–O(5A)	177.96(6)		
Li(1)–O(2)*	1.919(4)	O(2)–Fe(1)–O(6A)	92.14(6)		
Li(1)–O(3)**	2.096(4)	O(3)–Fe(1)–O(3A)	78.95(6)		
Li(1)–O(4)	1.838(4)	O(5A)–Fe(1)–O(1)	95.34(6)		
Li(1)–O(5)*	1.932(4)	O(5A)–Fe(1)–O(3)	97.00(6)		
		O(5A)–Fe(1)–O(3A)	80.99(6)		
		O(5A)–Fe(1)–O(6A)	86.28(6)		
		O(6A)–Fe(1)–O(3)	98.30(6)		
		O(6A)–Fe(1)–O(3A)	166.51(6)		

* – bridging oxygen; ** – chelating-bridging oxygen

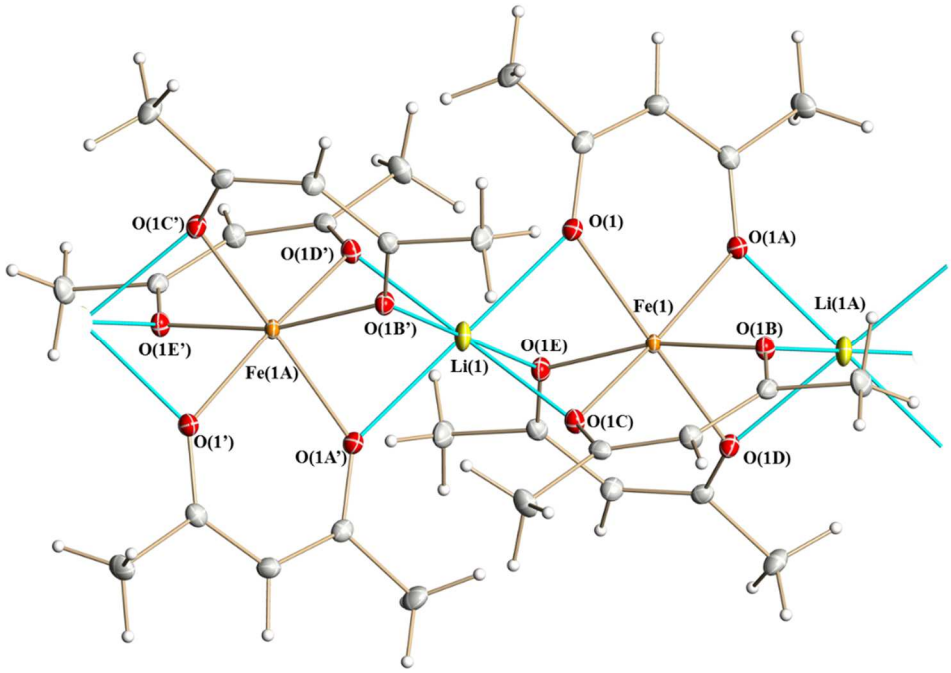

Figure S9. Fragment of the polymeric structure of $LiFe(acac)_3$ (**3**) drawn with thermal ellipsoids at the 40% probability level. Hydrogen atoms are represented by spheres of arbitrary radius. Only metal and oxygen atoms are labeled. The lithium-oxygen bonds to the acac ligands involved in bridging interactions are shown in blue.

Table S11. Selected Bond Distances (Å) and Angles (deg.) in the Structure of $LiFe(acac)_3$ (**3**)

Bond distances		**Angles**		**Angles**	
Fe(1)–O(1)**	2.070(2)	O(1)–Fe(1)–O(1A)	87.58(12)	O(1)–Li(1)–O(1A')	180.00(11)
Li(1)–O(1)*	2.155(2)	O(1)–Fe(1)–O(1B)	103.81(12)	O(1)–Li(1)–O(1B')	99.09(9)
		O(1)–Fe(1)–O(1C)	84.99(9)	O(1)–Li(1)–O(1C)	80.91(9)
		O(1)–Fe(1)–O(1D)	167.96(12)	O(1)–Li(1)–O(1D')	99.08(9)
		O(1)–Fe(1)–O(1E)	84.99(9)	O(1)–Li(1)–O(1E)	80.92(9)

** – chelating-bridging oxygen; *– bridging oxygen

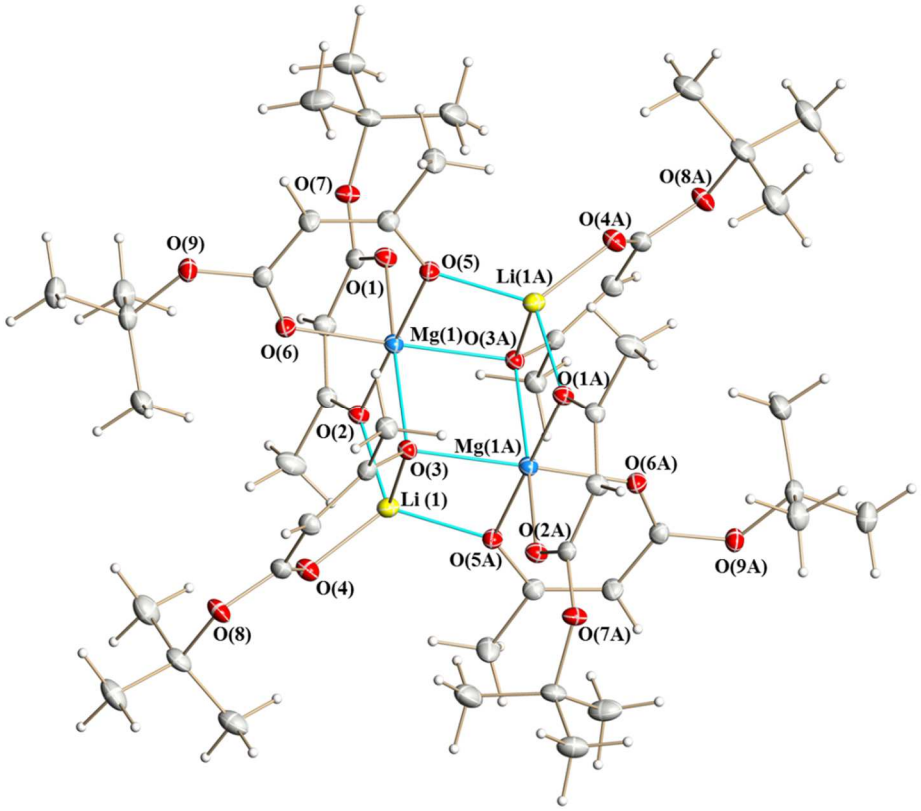

Figure S10. Solid state structure of heterometallic complex $Li_2Mg_2(tbaoac)_6$ (**4)** drawn with thermal ellipsoids at the 40% probability level. Hydrogen atoms are represented by spheres of arbitrary radius. Only metal and oxygen atoms are labeled. The lithium-oxygen and magnesium-oxygen bonds to the tbaoac ligands involved in bridging interactions are shown in blue.

Table S12. Selected Bond Distances (Å) and Angles (deg.) in the Structure of $Li_2Mg_2(tbaoac)_6$ (**4**)

Bond distances		**Angles**		**Angles**	
Mg(1)–O(1)	2.0300(17)	O(6)–Mg(1)–O(2)	94.22(6)	O(2)–Li(1)–O(3)	90.18(15)
Mg(1)–O(2)**	2.0253(16)	O(6)–Mg(1)–O(5)	86.26(6)	O(4)–Li(1)–O(2)	114.98(19)
Mg(1)–O(3)*	2.1355(17)	O(2)–Mg(1)–O(5)	179.24(7)	O(4)–Li(1)–O(3)	100.83(17)
Mg(1)–O(3A)*	2.1270(15)	O(6)–Mg(1)–O(1)	94.05(7)	O(4)–Li(1)–O(5A)	124.7(2)
Mg(1)–O(5)**	2.0300(16)	O(2)–Mg(1)–O(1)	86.07(6)	O(5A)–Li(1)–O(2)	118.93(19)
Mg(1)–O(6)	2.0240(16)	O(5)–Mg(1)–O(1)	93.31(7)	O(5A)–Li(1)–O(3)	90.67(15)
		O(6)–Mg(1)–O(3A)	166.24(6)		
Li(1)–O(2)*	1.892(4)	O(2)–Mg(1)–O(3A)	96.96(6)		
Li(1)–O(3)**	1.974(4)	O(5)–Mg(1)–O(3A)	82.65(6)		
Li(1)–O(4)	1.829(4)	O(1)–Mg(1)–O(3A)	94.69(7)		
Li(1)–O(5A)*	1.886(4)	O(6)–Mg(1)–O(3)	92.98(7)		
		O(2)–Mg(1)–O(3)	82.27(6)		
		O(5)–Mg(1)–O(3)	98.30(6)		
		O(1)–Mg(1)–O(3)	166.79(6)		
		O(3)–Mg(1)–O(3A)	80.65(7)		

* – bridging oxygen; ** – chelating-bridging oxygen

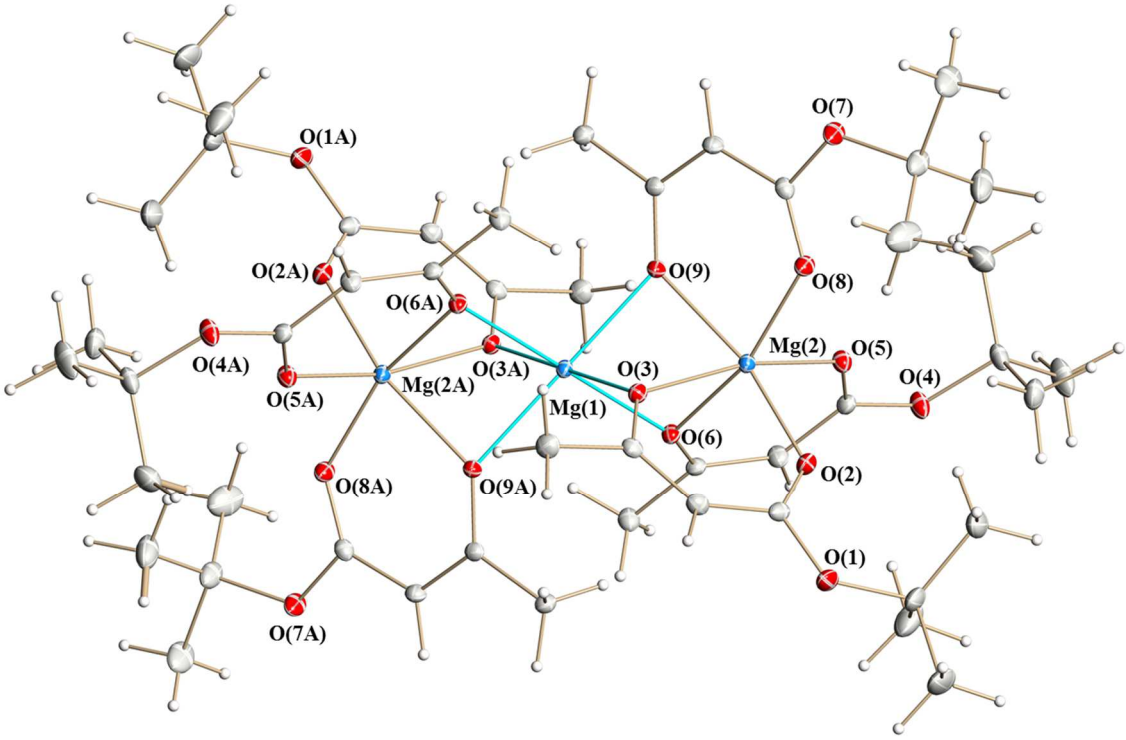

Figure S11. Solid state structure of homometallic complex $Mg_3(tbaoac)_6$ drawn with thermal ellipsoids at the 40% probability level. Hydrogen atoms are represented by spheres of arbitrary radius. Only metal and oxygen atoms are labeled. The magnesium-oxygen bonds to the tbaoac ligands involved in bridging interactions are shown in blue.

Table S13. Selected Bond Distances (Å) and Angles (deg.) in the Structure of $Mg_3(tbaoac)_6$

Bond distances		**Angles**		**Angles**	
Mg(1)–O(3)*	2.0732(9)	O(6)–Mg(1)–O(3)	79.78(3)	O(2)–Mg(2)–O(3)	85.76(4)
Mg(1)–O(6)*	2.0707(9)	O(6)–Mg(1)–O(3A)	100.22(4)	O(2)–Mg(2)–O(5)	91.03(4)
Mg(1)–O(9)*	2.0660(9)	O(6A)–Mg(1)–O(3A)	79.78(3)	O(2)–Mg(2)–O(6)	99.62(4)
		O(9)–Mg(1)–O(3)	78.76(4)	O(2)–Mg(2)–O(9)	163.81(5)
Mg(2)–O(2)	2.0142(11)	O(9)–Mg(1)–O(3A)	101.24(4)	O(5)–Mg(2)–O(3)	165.40(4)
Mg(2)–O(3)**	2.0874(10)	O(9)–Mg(1)–O(6)	78.61(3)	O(5)–Mg(2)–O(6)	87.23(4)
Mg(2)–O(5)	2.0173(10)	O(9)–Mg(1)–O(6A)	101.39(3)	O(5)–Mg(2)–O(9)	104.78(4)
Mg(2)–O(6)**	2.0774(10)	O(9A)–Mg(1)–O(3)	101.24(4)	O(6)–Mg(2)–O(3)	79.30(4)
Mg(2)–O(8)	2.0003(10)	O(9A)–Mg(1)–O(3A)	78.76(4)	O(6)–Mg(2)–O(9)	78.07(4)
Mg(2)–O(9)**	2.0830(10)	O(9A)–Mg(1)–O(6)	101.39(3)	O(8)–Mg(2)–O(2)	97.01(4)
		O(9A)–Mg(1)–O(6A)	78.61(3)	O(8)–Mg(2)–O(3)	102.77(4)
				O(8)–Mg(2)–O(5)	91.75(4)
				O(8)–Mg(2)–O(6)	163.36(4)
				O(8)–Mg(2)–O(9)	86.15(4)
				O(9)–Mg(2)–O(3)	78.06(4)

* – bridging oxygen; ** – chelating-bridging oxygen

ATR-IR Spectra of Heterometallic Compounds 1-4

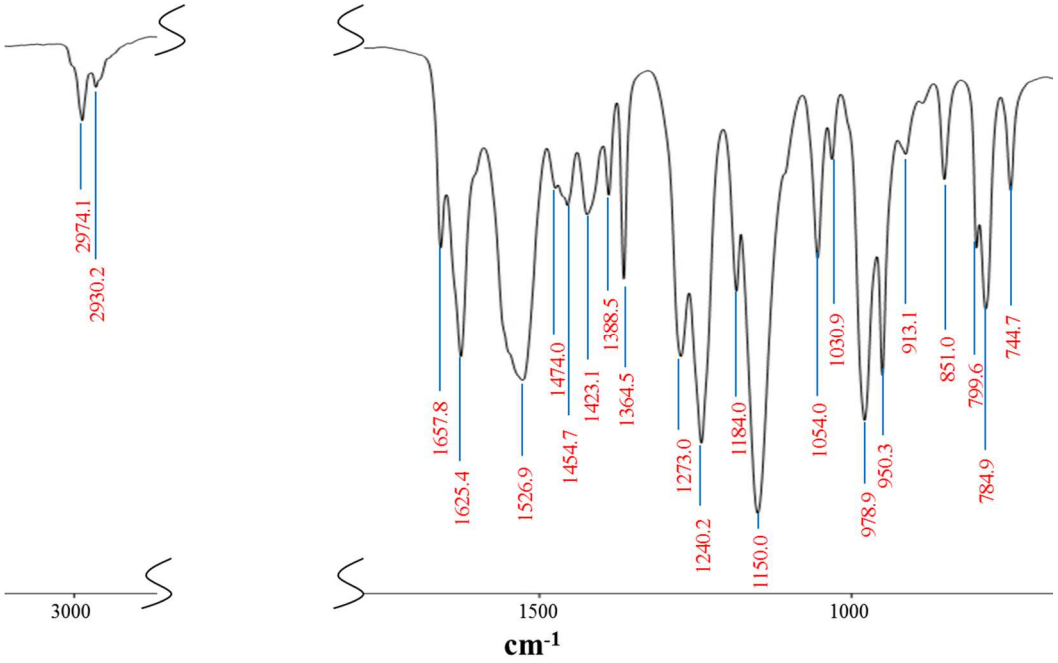

Figure S12. The attenuated total reflection (ATR) spectrum of $LiFe(tbaoac)_3$ (**1**).

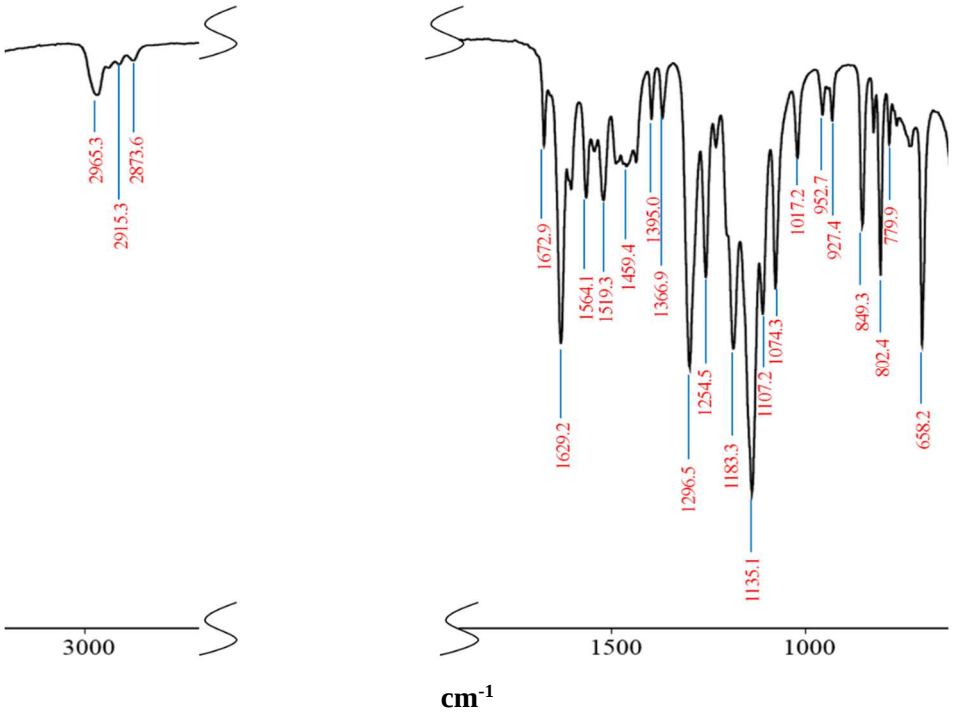

Figure S13. The attenuated total reflection (ATR) spectrum of $LiFe(ptac)_3$ (**2**).

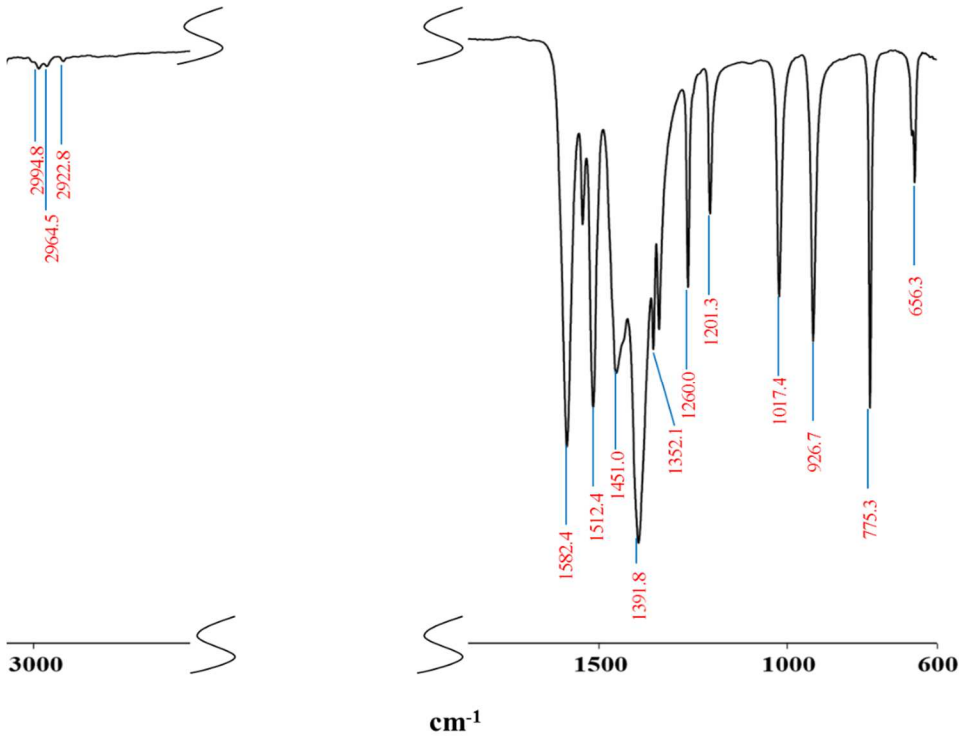

Figure S14. The attenuated total Reflection (ATR) spectrum of $LiFe(acac)_3$ (**3**).

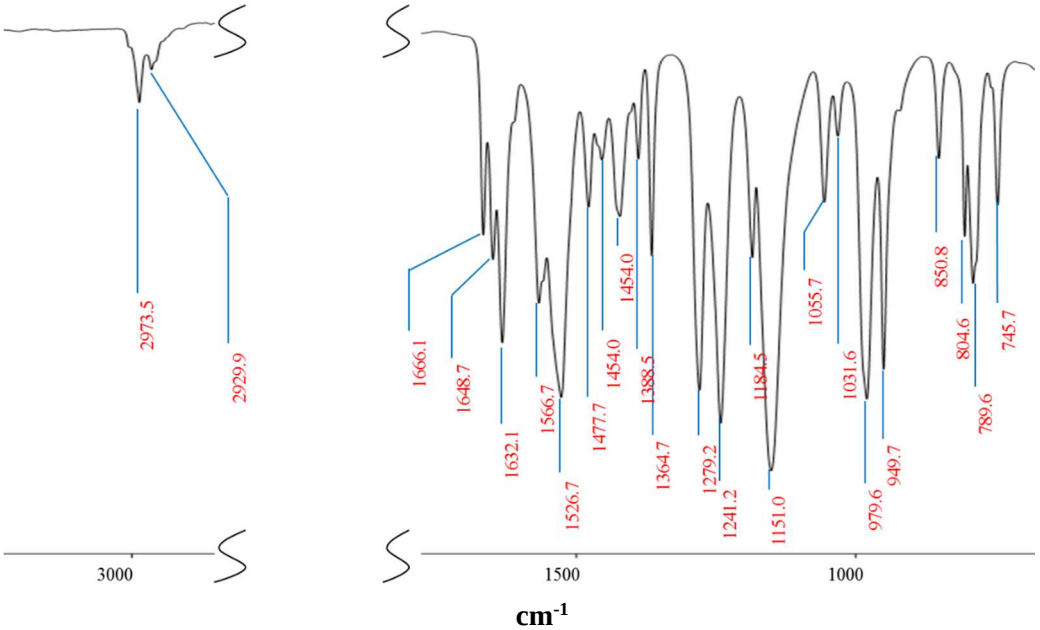

Figure S15. The attenuated total reflection (ATR) spectrum of $LiMg(tbaoac)_3$ (**4**).

^{1}H and ^{7}Li NMR Spectra of LiMg(tbaoac)$_3$ (4)

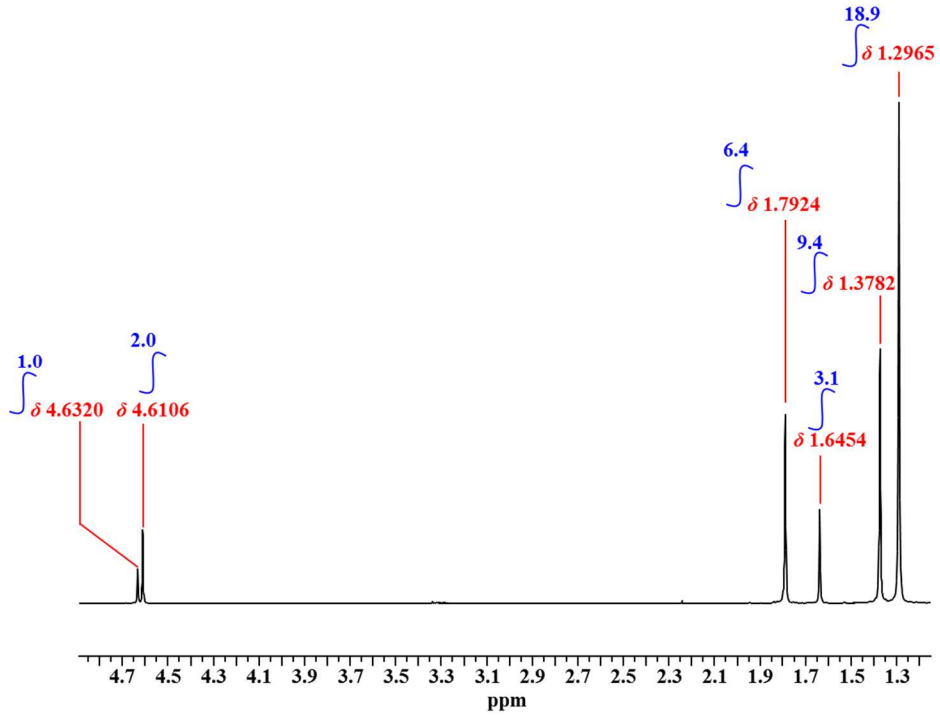

Figure S16. ^{1}H NMR spectrum of LiMg(tbaoac)$_3$ (**4**) in $CDCl_3$ recorded at room temperature.

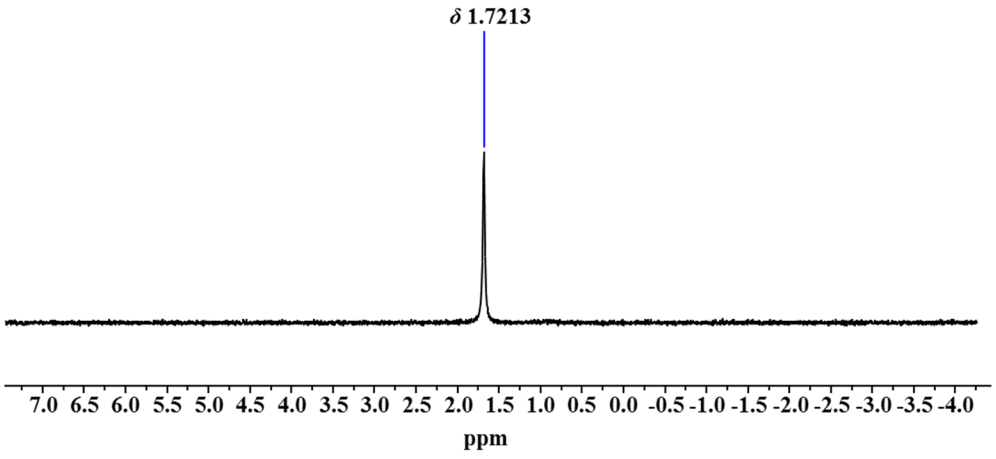

Figure S17. ^{7}Li NMR spectrum of LiMg(tbaoac)$_3$ (**4**) in $CDCl_3$ recorded at room temperature. Chemical shift was calibrated based on the external standard LiCl in D_2O.

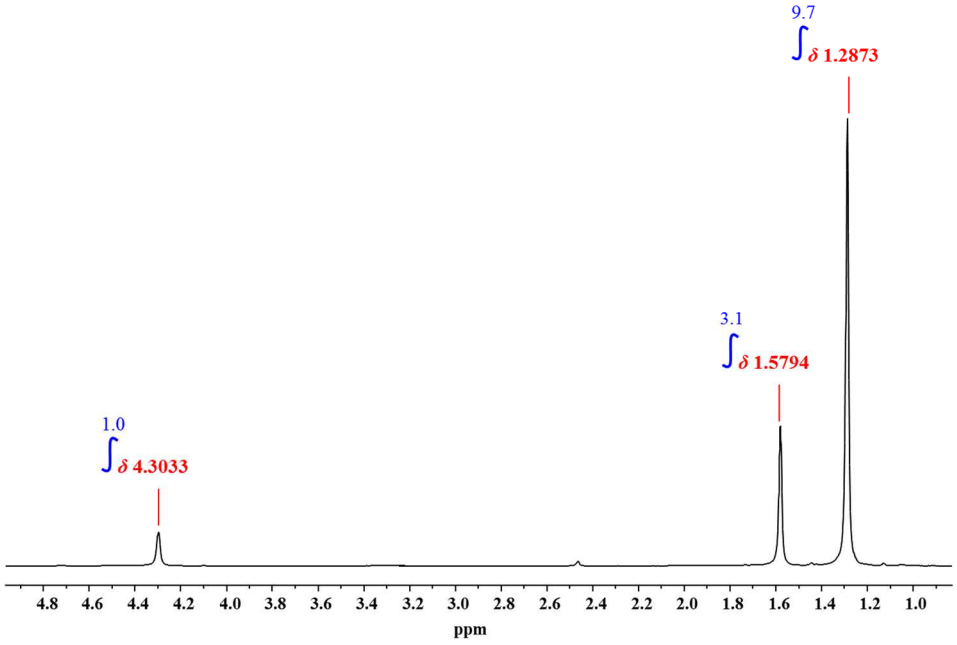

Figure S18. ^{1}H NMR spectrum of LiMg(tbaoac)$_3$ (**4**) in d_6-DMSO recorded at room temperature.

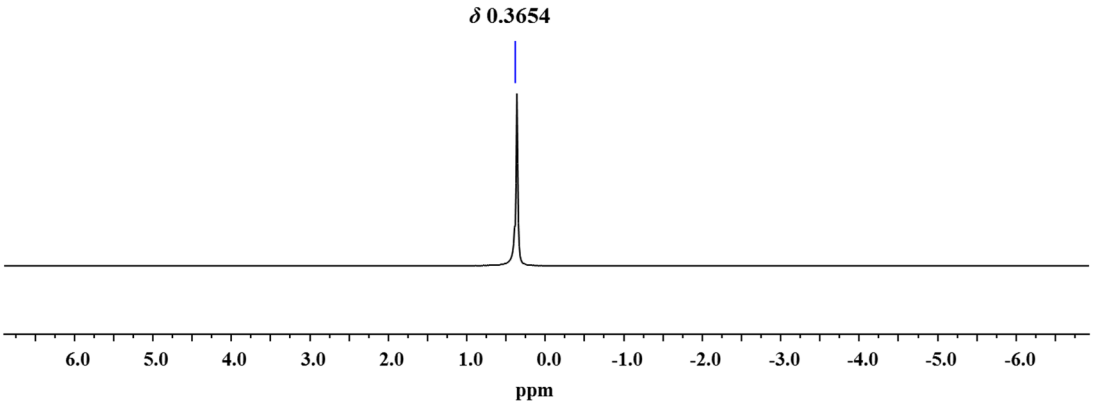

Figure S19. ^{7}Li NMR spectrum of LiMg(tbaoac)$_3$ (**4**) in d_6-DMSO recorded at room temperature. Chemical shift was calibrated based on the external standard LiCl in D_2O.

DART Mass Spectra of Heterometallic Compounds 1, 2, and 4

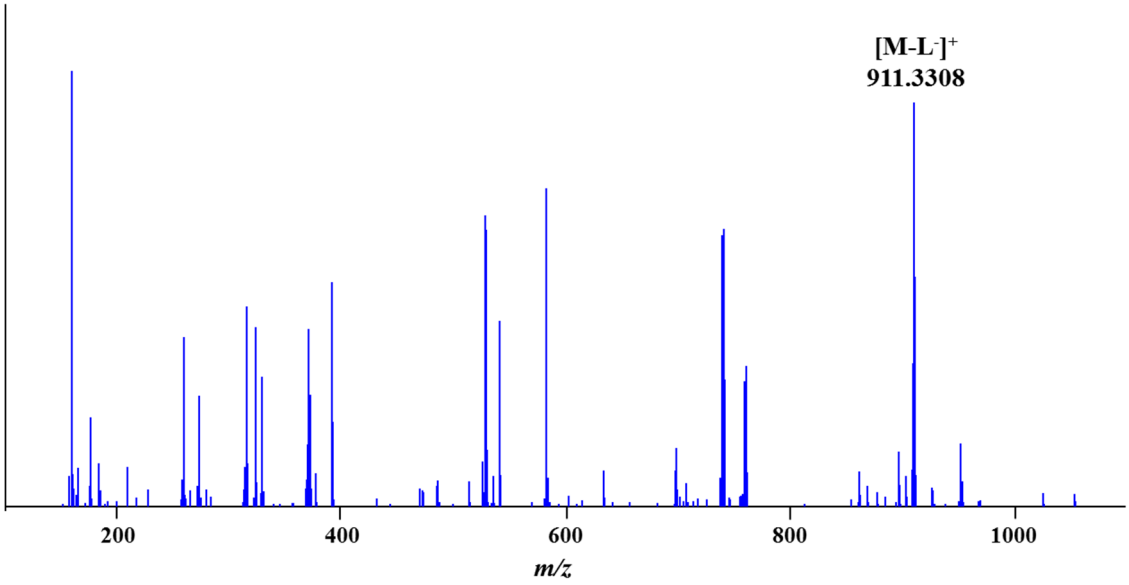

Figure S20. Positive-ion DART mass spectrum of solid $LiFe(tbaoac)_3$ (**1**).

Table S14. Assignment of Ions Detected in Positive-Ion DART Mass Spectrum of $LiFe(tbaoac)_3$ (**1**) (M = $Li_2Fe_2(tbaoac)_6$, L = tbaoac = $C_8H_{13}O_3$)

Ions	Measured *m/z*	Calculated *m/z*	*Δ*	% Base
$[Li_2Fe_2L_5]^+$	911.3308	911.3342	-0.0034	92.8
$[Fe_2L_4+H]^+$	741.2197	741.2236	-0.0039	64.4
$[Fe_2L_3]^+$	583.1124	583.1293	-0.0169	73.6
$[Li_2FeL_3]^+$	541.2201	541.2264	-0.0063	43.4
$[LiFeL_2]^+$	377.1183	377.1239	-0.0056	9.1
$[HL+H]^+$	159.1013	159.1021	0.0008	100

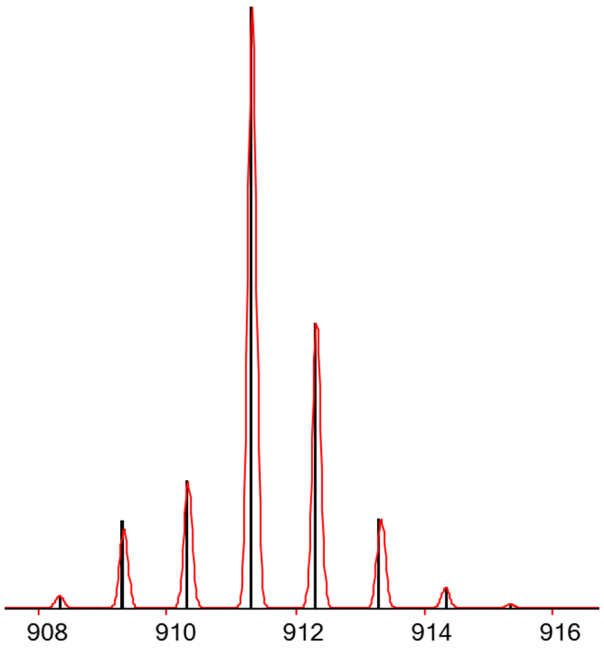

Figure S21. Isotope distribution pattern for the $[M\text{-}L]^+$ peak (M = $Li_2Fe_2(tbaoac)_6$).

Table S15. Assignment of $[M\text{-}L]^+$ Ions Detected in Positive-Ion DART Mass Spectrum of Solid $LiFe(tbaoac)_3$ (**1**) (M = $Li_2Fe_2(tbaoac)_6$, L = tbaoac = $C_8H_{13}O_3$)

Ion	**Measured *m/z***	**Calculated *m/z***	**Experimental Abundance (%)**	**Theoretical Abundance (%)**	***Δ***
$[M\text{-}L]^+$	909.3341	909.3389	14.2	12.7	-0.0048
	910.3287	910.3333	17.3	16.4	-0.0046
	911.3308	911.3342	100	100	-0.0034
	912.3331	912.3376	41.4	43.3	-0.0045
	913.3347	913.3409	10.5	9.1	-0.0062

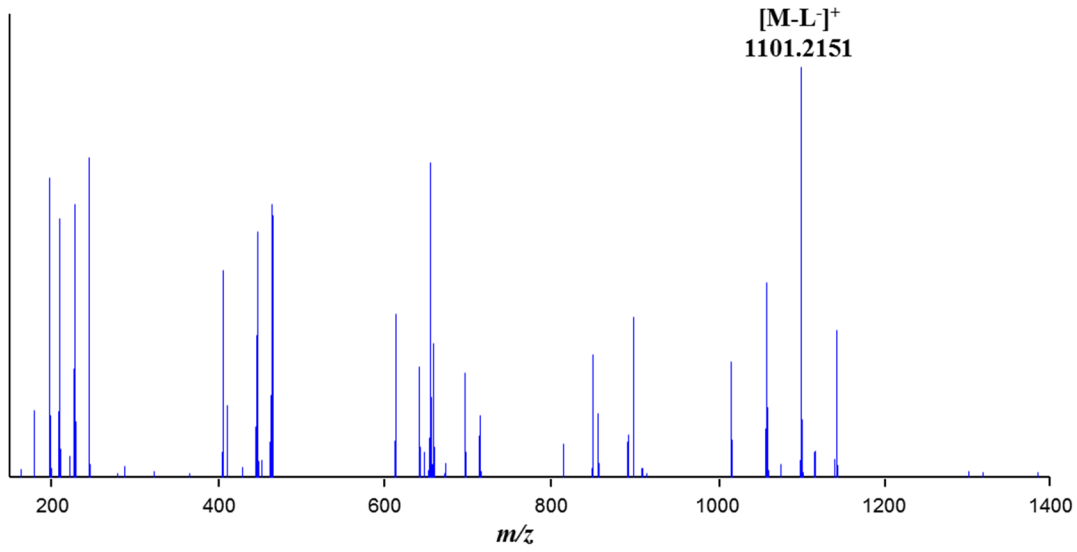

Figure S22. Positive-ion DART mass spectrum of solid $LiFe(ptac)_3$ (**2**).

Table S16. Assignment of Ions Detected in Positive-Ion DART Mass Spectrum of $LiFe(ptac)_3$ (**2**) (M = $Li_2Fe_2(ptac)_6$, L = ptac = $C_8H_{10}F_3O_2$)

Ions	Measured *m/z*	Calculated *m/z*	*Δ*	% Base
$[Li_3Fe_2L_6]^+$	1303.2943	1303.2976	-0.0033	4.67
$[Li_2Fe_2L_5]^+$	1101.2151	1101.2183	-0.0032	100
$[LiFe_2L_4]^+$	899.1308	899.1390	-0.0082	41.19
$[Fe_2L_4+H]^+$	893.1204	893.1309	-0.0105	13.45
$[Fe_2L_3]^+$	697.0542	697.0597	-0.0055	27.89
$[Li_2FeL_3]^+$	655.1573	655.1568	0.0005	77.75
$[LiFeL_2]^+$	453.0816	453.0775	0.0041	7.45
$[Li_2L]^+$	405.1651	405.1664	-0.0013	52.41
$[LH+H]^+$	197.0822	197.0789	0.0033	73.99

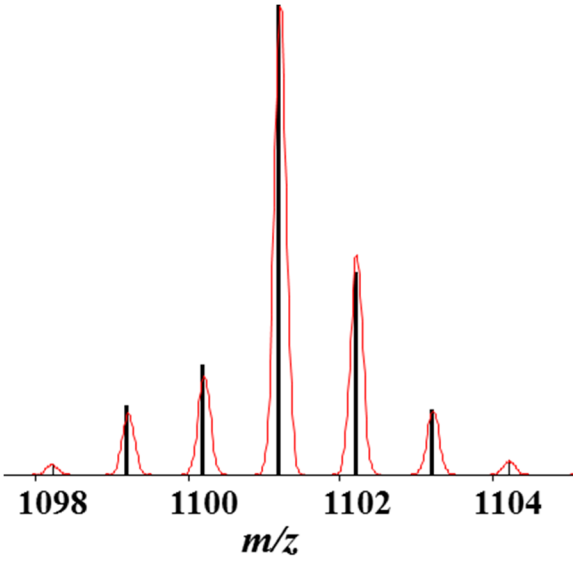

Figure S23. Isotope distribution pattern for the $[M\text{-}L]^+$ peak (M = $Li_2Fe_2(ptac)_6$).

Table S17. Assignment of $[M\text{-}L]^+$ Ions Detected in Positive-Ion DART Mass Spectrum of $LiFe(ptac)_3$ (**2**) (M = $Li_2Fe_2(ptac)_6$, L = ptac = $C_8H_{10}F_3O_2$)

Ion	**Measured *m/z***	**Calculated *m/z***	**Experimental Abundance (%)**	**Theoretical Abundance (%)**	***Δ***
$[M\text{-}L]^+$	1099.2195	1099.2230	14.2	12.7	-0.0035
	1100.2168	1100.2174	17.2	16.4	-0.0006
	1101.2151	1101.2183	100	100	-0.0032
	1102.2189	1102.2217	41.2	43.3	-0.0028
	1103.2192	1103.2250	9.0	9.1	-0.0058

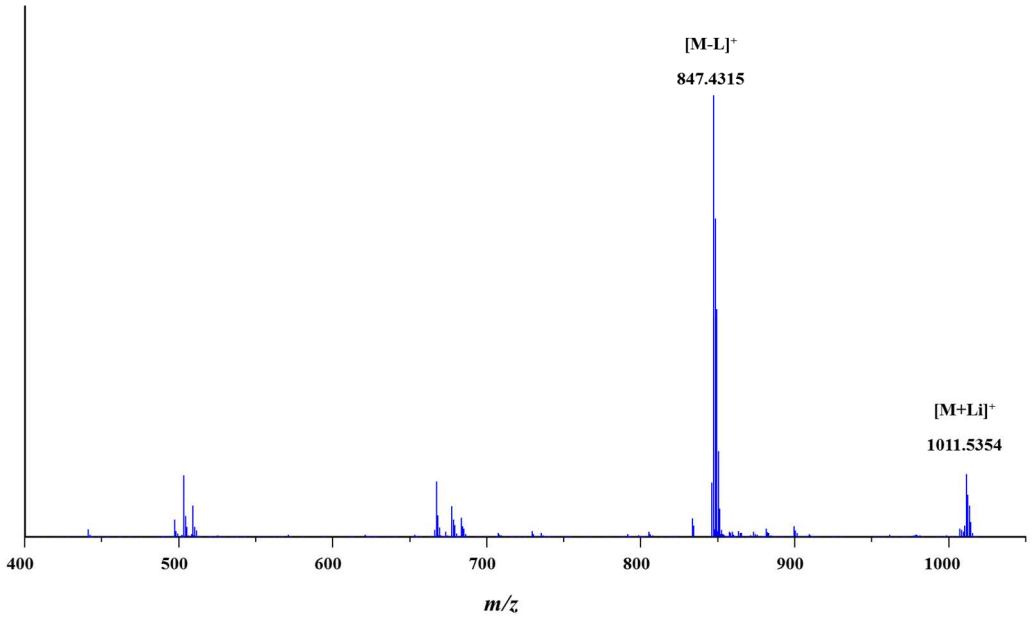

Figure S24. Positive-ion DART mass spectrum of solid $LiMg(tbaoac)_3$ (**4**).

Table S18. Assignment of Ions Detected in Positive-Ion DART Mass Spectrum of $LiMg(tbaoac)_3$ (**4**) (M = $Li_2Mg_2(tbaoac)_6$, L = tbaoac = $C_8H_{13}O_3$)

Ions	Measured *m/z*	Calculated *m/z*	*Δ*	% Base
$[Li_3Mg_2L_6]^+$	1011.5354	1011.5369	-0.0015	14.30
$[Li_2Mg_2L_5]^+$	847.4315	847.4346	-0.0031	100
$[LiMg_2L_4]^+$	683.3317	683.3320	-0.0003	4.42
$[Mg_2L_4+H]^+$	677.3282	677.3238	0.0044	6.99
$[Li_2MgL_4+H]^+$	667.3693	667.3708	-0.0015	12.59
$[Li_2MgL_3]^+$	509.2832	509.2765	0.0067	7.12
$[LiMgL_3+H]^+$	503.2744	503.2683	0.0061	13.96

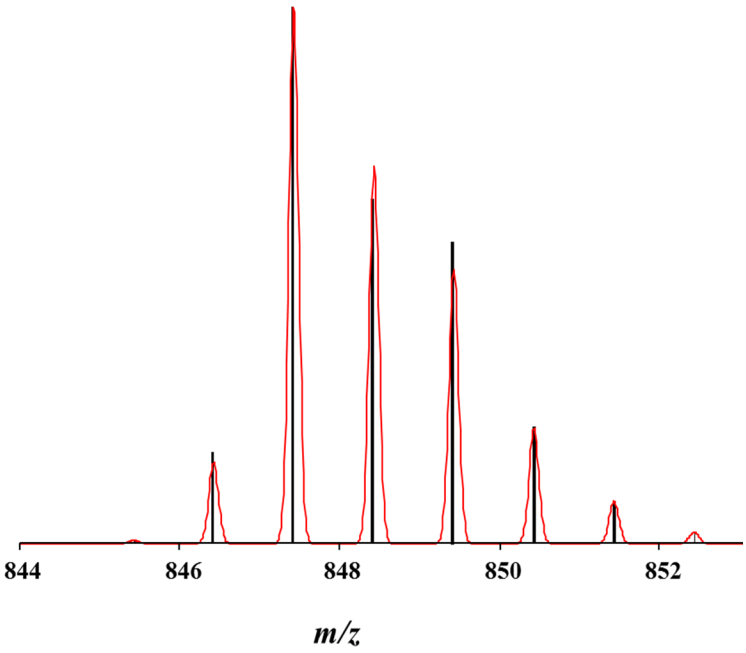

Figure S25. Isotope distribution pattern for the $[M-L]^+$ peak (M = $Li_2Mg_2(tbaoac)_6$).

Table S19. Assignment of $[M-L]^+$ Ions Detected in Positive-Ion DART Mass Spectrum of $LiMg(tbaoac)_3$ (**4**) (M = $Li_2Mg_2(tbaoac)_6$, L = tbaoac = $C_8H_{13}O_3$)

Ion	Measured *m/z*	Calculated *m/z*	Experimental Abundance (%)	Theoretical Abundance (%)	*Δ*
$[M-L]^+$	846.4321	846.4336	18.5	15.1	-0.0015
	847.4315	847.4346	100	100	-0.0029
	848.4347	848.4367	68.4	70.5	-0.0020
	849.4305	849.4356	23.1	19.0	-0.0051
	850.4367	850.4369	21.4	21.5	-0.0002
	851.4353	851.4369	6.7	7.9	-0.0016

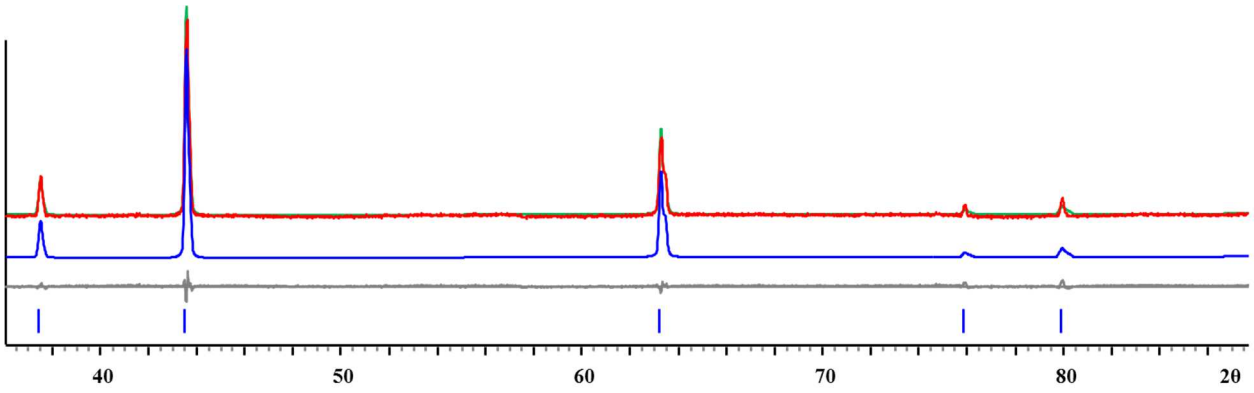

Figure S26. X-ray powder diffraction pattern of α-$LiFeO_2$ obtained by thermal decomposition of heterometallic precursor $LiFe(tbaoac)_3$ (**1**) at 600 °C in air. The red and green lines are experimental and calculated patterns overlaid. Blue curve is a calculated pattern. Grey line is the difference curve. Theoretical peak positions are shown at the bottom as blue lines.

Table S20. Comparison of the Unit Cell Parameters for α-$LiFeO_2$ Oxide Obtained by Thermal Decomposition of Heterometallic Precursor $LiFe(tbaoac)_3$ (**1**) with the Literature Data

α-$LiFeO_2$		
	Le Bail Fit Results	Literature Data[3]
Sp. Gr.	*Fm*-3*m*	
a (Å)	4.1618(1)	4.1620(3)

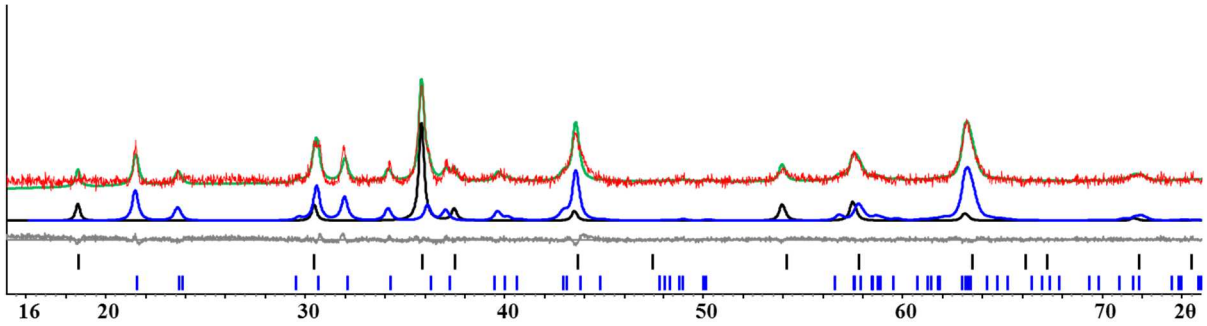

Figure S27. X-ray powder diffraction pattern of the residue obtained by thermal decomposition of heterometallic precursor $LiFe(tbaoac)_3$ (**1**) at 550 °C in air. The red and green curves are experimental and calculated patterns overlaid. The black and blue curves are calculated single peak patterns for $LiFe_5O_8$ and Li_2CO_3 with theoretical peak positions shown at the bottom as black and blue lines, respectively. Grey line is the difference curve.

Table S21. Comparison of the Unit Cell Parameters for Li_2CO_3 and $LiFe_5O_8$ Obtained by Thermal Decomposition of Heterometallic Precursor $LiFe(tbaoac)_3$ (**1**) with the Literature Data

	Li_2CO_3		$LiFe_5O_8$	
	LeBail Fit	Literature Data[4]	LeBail Fit	Literature Data[5]
Sp. Gr.	*C*2/*c*		*P*4$_3$32	
a (Å)	8.3592(2)	8.39*	8.3328(1)	8.3339(1)
b (Å)	4.9714(2)	5.00		
c (Å)	6.1971(2)	6.21		
β (°)	113.992(6)	114.5		

* no standard deviations reported.

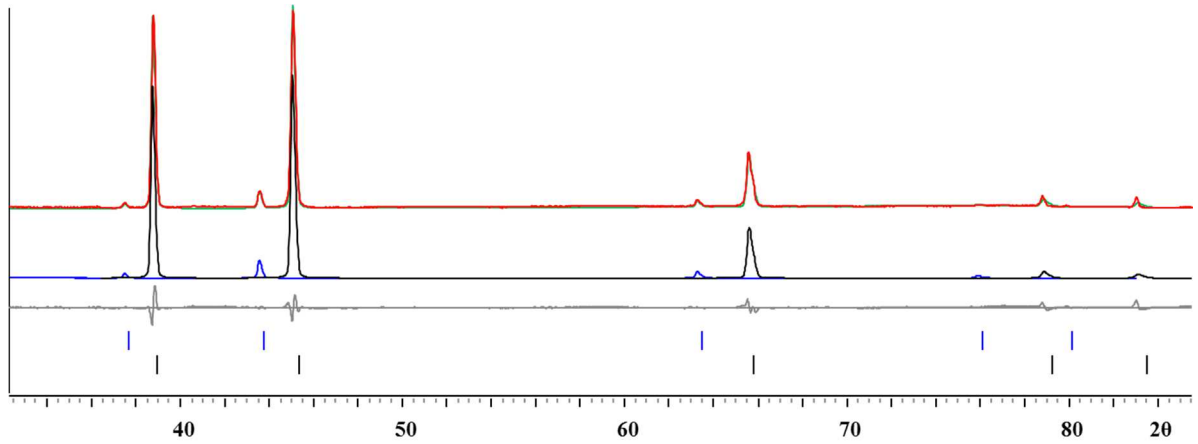

Figure S28. X-ray powder diffraction pattern of the residue obtained by thermal decomposition of heterometallic precursor $LiFe(ptac)_3$ (**2**) at 750 °C in air. The red and green curves are experimental and calculated patterns overlaid. The black and blue curves are calculated single peak patterns for LiF and $LiFeO_2$ with theoretical peak positions shown at the bottom as black and blue lines, respectively. Grey line is the difference curve.

Table S22. Comparison of the Unit Cell Parameters for LiF and $LiFeO_2$ Obtained by Thermal Decomposition of Heterometallic Precursor $LiFe(ptac)_3$ (**2**) with the Literature Data

	LiF		$LiFeO_2$	
	LeBail Fit	Literature Data[6]	LeBail Fit	Literature Data[3]
Sp. Gr.	*Fd*-3*m*		*Fd*-3*m*	
a (Å)	4.0269(2)	4.0272(2)	4.1655(2)	4.1620(3)

References

1. Z. Wei, H. Han, A. S. Filatov and E. V. Dikarev, *Chem. Sci.*, **2014**, 5, 813-818.
2. E. S. Filatov, I. A. Baidina and I. K. Igumenov, *J. Struct. Chem.*, **2006**, 47, 484-488.
3. M. Tabuchi, K. Ado, H. Kobayashi, I. Matsubara, H. Kageyama, M. Wakita, S. Tsutsui, S. Nasu, Y. Takeda, C. Masquelier, A. Hirano and R. Kanno, *J. Solid State Chem.*, **1998**, 141, 554-561.
4. J. Zemann, *Acta Crystallogr.*, **1957**, 10, 664-666.
5. A. I. Smolentsev, A. B. Meshalkin, N. V. Podberezskaya and A. B. Kaplun, *J. Struct. Chem.*, **2008**, 49, 953-956.
6. C. J. Kim, M. J. Kim, J. M. Yang and I. H. Suh, *Chungnam Kwahak Yonguchi*, **1985**, 12, 59-64.